



ELSEVIER

Contents lists available at ScienceDirect

Catalysis Today

journal homepage: www.elsevier.com/locate/cattod

Effect of transition metal oxide doping on catalytic activity of titania for the oxidation of 1,2-dichloroethane

Xing Zhang, Yuxi Liu*, Jiguang Deng, Lin Jing, Xiaohui Yu, Zhuo Han, Hongxing Dai*

Beijing Key Laboratory for Green Catalysis and Separation, Key Laboratory of Beijing on Regional Air Pollution Control, Key Laboratory of Advanced Functional Materials, Education Ministry of China, Laboratory of Catalysis Chemistry and Nanoscience, Department of Chemistry and Chemical Engineering, College of Environmental and Energy Engineering, Beijing University of Technology, Beijing 100124, China

ARTICLE INFO

Keywords:

Titania
Transition metal oxide
Supported catalyst
Chlorinated volatile organic compound
1,2-Dichloroethane oxidation

ABSTRACT

Transition metal oxides (MO_x ; $M = \text{Cr, Mn, Fe, Ni, Cu}$)-doped titania solid solution catalysts (10 wt% $\text{MO}_x\text{-TiO}_2$, denoted as $10\text{MO}_x\text{-TiO}_2$) were prepared by the coprecipitation method. The techniques of XRD, TPR, TPD, XPS, TPSR, and in situ DRIFTS were used to characterize physicochemical properties of the materials, and their catalytic activities were evaluated for the oxidation of 1,2-dichloroethane (1,2-DCE). The introduction of MO_x enhanced adsorption and activation of oxygen molecules, mobility of surface lattice oxygen, and low-temperature reducibility. The $10\text{MO}_x\text{-TiO}_2$ catalysts showed good performance, with $10\text{CrO}_x\text{-TiO}_2$ exhibiting the highest catalytic activity (reaction rate = $2.35 \times 10^{-7} \text{ mol}/(\text{g}_{\text{cat}} \text{ s})$) and apparent activation energy (E_a) = 35 kJ/mol at space velocity = 40,000 mL/(g h) and good resistance to chlorine poisoning. The mechanism of 1,2-DCE oxidation over $10\text{CrO}_x\text{-TiO}_2$ was also discussed based on the results of TPSR and in situ DRIFTS characterization. It is concluded that strong acidity and redox ability, high adsorbed oxygen species concentration, and strong interaction between TiO_2 and CrO_x were accountable for the good performance of $10\text{CrO}_x\text{-TiO}_2$.

1. Introduction

Most of volatile organic compounds (VOCs), especially chlorinated VOCs (CVOCs) produced in industrial production processes, are harmful to the atmosphere and human health [1–4]. Typical CVOCs, such as 1,2-dichloroethane (1,2-DCE), trichloroethylene (TCE), and chlorobenzene (CB) are of high toxicity and long-term persistence. Catalytic oxidation is believed to be the most effective pathway for CVOCs removal, in which the critical issue is the development of new catalysts with superior activity and stability and without secondary pollutants generation. Theoretically, CVOCs are completely eliminated via the formation of HCl, CO_2 , and H_2O and dissociation of the C–Cl bonds. In fact, interaction of chlorine-containing products with the catalyst can lead to its deactivation, which is a major problem in the oxidation of CVOCs, and the poisoning can block the active sites and hence decrease the performance of a catalyst. Therefore, the catalyst plays an important role in effective removal of CVOCs. Generally speaking, there are two types of catalysts (i.e., supported noble metals and (mixed) metal oxides) for deep oxidation of CVOCs [5]. The supported noble metal catalysts often exhibit good low-temperature activity, but their wide applications are restricted due to high cost and easy deactivation by Cl poisoning. However, the cheap transition metal

oxide catalysts have drawn much attention owing to good activity for CVOCs oxidation as well as good resistance to Cl poisoning [6]. Recently, there have been some reports on catalytic elimination of CVOCs. For instance, Gu et al. [7] synthesized the $\text{Ru/Ce}_x\text{Al}_y$ catalysts using the impregnation method, and found that (i) reducibility and acidity of the catalyst increased with a rise in $\text{Ce}/(\text{Ce} + \text{Al})$ molar ratio; (ii) $\text{Ce}_{25}\text{Al}_{75}$ showed the highest catalytic activity (TOF_{Ce} was $0.79 \mu\text{mol}/(\text{m}^2 \text{ min})$); (iii) the $T_{50\%}$ and $T_{90\%}$ for 1,2-DCE oxidation over 1.8 wt% $\text{Ru/Ce}_x\text{Al}_y$ ($\text{Ce}/(\text{Ce} + \text{Al})$ molar ratio = 0.10–0.25) at space velocity (SV) = $30,000 \text{ h}^{-1}$ were 287 and 322 °C, respectively; and (iv) $\text{Ru/Ce}_{10}\text{Al}_{90}$ exhibited good stability with 99 % CO_2 selectivity at 280 °C within 25 h of on-stream reaction. Chen et al. [8] pointed out that the $\text{Pt}/\text{Al}_2\text{O}_3\text{-CeO}_2$ catalyst was active and durable for dichloromethane oxidation. Wang and coworkers [9] prepared the $\text{Ru}/\text{Co}_3\text{O}_4$ catalysts via a wet impregnation method and explored their catalytic elimination of 1,2-dichlorobenzene. The $\text{Ru}/\text{Co}_3\text{O}_4$ catalysts exhibited good activity and selectivity with the reaction rate of $9.4\text{--}9.8 \mu\text{mol}/(\text{m}^2 \text{ min})$. Dai et al. [10] generated the CeO_2 nanobelts using an aqueous-phase precipitation strategy and loaded VO_x on the CeO_2 nanobelts using an incipient-wetness impregnation method. The authors claimed that 6.0 wt% VO_x/CeO_2 nanobelts exhibited an excellent catalytic activity ($T_{90\%} = 240 \text{ °C}$ at SV = $15,000 \text{ mL}/(\text{g h})$) in the combustion of 1,2-

* Corresponding authors.

E-mail addresses: yxliu@bjut.edu.cn (Y. Liu), hxdai@bjut.edu.cn (H. Dai).

<https://doi.org/10.1016/j.cattod.2019.12.011>

Received 17 September 2019; Received in revised form 25 November 2019; Accepted 2 December 2019

0920-5861/ © 2019 Elsevier B.V. All rights reserved.

DCE. Yang et al. [11] prepared cerium-transition metal mixed oxides (4Ce1M, M = V, Cr, Mn, Fe, Co, Ni, and Cu) by the coprecipitation method, investigated catalytic properties of these materials for deep oxidation of four typical CVOCs, and found that the 4Ce1Cr catalyst possessed the optimal activity ($T_{90\%} = 232\text{ }^\circ\text{C}$ at SV = 15,000 h⁻¹) and selectivity, which was mainly associated with strong oxidizing ability of the Cr⁶⁺ species. After investigating the (Ce,Cr)_xO₂/MO_y (M = Ti, V, Nb, Mo, W, and La) catalysts for total oxidation of 1,2-DCE, Zhou and coworkers [12] concluded that the improved redox property and increased surface Ce³⁺ and Cr⁶⁺ species contents enhanced oxidation performance of the catalyst, in which (Ce,Cr)_xO₂/Nb₂O₅ performed the best ($T_{90\%} = 225\text{ }^\circ\text{C}$ at SV = 9000 mL/(g h)).

During the oxidation process of CVOCs, the Cl-containing inorganic species (HCl and/or Cl₂) are easily adsorbed on the surface of a catalyst or react with the active species to form volatile metal chlorides, resulting in partial or even complete deactivation of the catalyst. The mixed transition metal oxide catalysts are expected to solve this problem. Introduction of a certain amount of transition metal (M = Cr, Mn, Fe, Ni or Cu) oxide is a useful strategy in modifying physicochemical properties and improving thermal stability of the TiO₂-based materials. The synergistic action between MO_x and TiO₂ and formation of oxygen vacancies in TiO₂ due to partial replacement of Ti⁴⁺ by Mⁿ⁺ could enhance activity and Cl-resistant stability of the MO_x-TiO₂ catalysts for the oxidative removal of CVOCs. Owing to the advantages (e.g., nontoxicity, cheapness, corrosion resistance, and long-term stability) of TiO₂, the TiO₂-based materials possessed highly selective and anti-poisoning properties in CVOCs deep oxidation [13,14].

In this work, we prepared the MO_x-TiO₂ (M = Cr, Mn, Fe, Ni, and Cu) mixed oxide catalysts using the coprecipitation method, characterized their physicochemical properties, measured their catalytic activities for deep oxidation of 1,2-DCE, examined impact of water vapor or hydrochloric acid on catalytic performance of the typical samples, and probed the involved oxidation mechanisms.

2. Experimental

2.1. Catalyst preparation

The 10 wt% MO_x-TiO₂ (M = Cr, Mn, Fe, Ni, and Cu) mixed oxide catalysts were prepared using the coprecipitation method. 1.0 g of tetrabutyl titanate and a desired amount of Cr(NO₃)₃, Mn(NO₃)₂, Fe(NO₃)₃, Ni(NO₃)₂ or Cu(NO₃)₂ were dissolved in 20 ml of ethanol aqueous solution (deionized water/ethanol volumetric ratio = 1 : 9). A certain amount of NH₄OH (1.0 mol/L)-ethanol aqueous solution was added dropwise into the above mixed solution at 50 °C under vigorous stirring for 8 h, in which the pH was adjusted to 10.0. The precipitated solids were filtered, washed with deionized water and ethanol three times, dried at 80 °C overnight, and calcined in air at 500 °C for 5 h, thus obtaining the 10 wt% MO_x-TiO₂ (denoted as 10MO_x-TiO₂) samples.

2.2. Catalyst characterization

The XRD, TEM, HAADF-STEM, elemental mapping, BET, XPS, H₂-TPR, O₂-TPD, NH₃-TPD, and CO₂-TPD, TPSR, and in situ DRIFTS techniques were used to characterize physicochemical properties of the samples. The detailed characterization procedures are described in the Supplementary material.

2.3. Catalytic activity evaluation

A continuous flow fixed-bed quartz microreactor (i.d. = 6 mm) was employed to evaluate catalytic activities of the samples for the oxidation of 1,2-DCE. To avoid the presence of hot spots, the sample (50 mg, 40–60 mesh) was mixed with quartz sand (0.25 g, 40–60 mesh). The total flow of the reactant feed of 1000 ppm 1,2-DCE + 20 vol% O₂ + N₂ (balance) was 33.4 mL/min, and the SV was ca. 40,000 mL/(g h). The

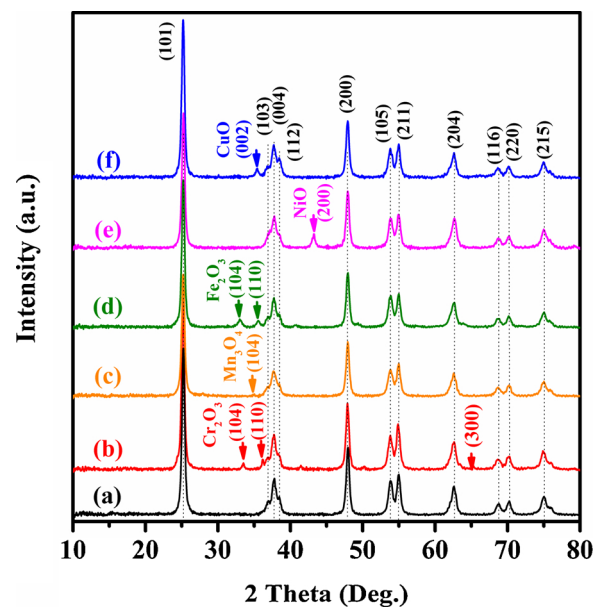


Fig. 1. XRD patterns of (a) TiO₂, (b) 10CrO_x-TiO₂, (c) 10MnO_x-TiO₂, (d) 10FeO_x-TiO₂, (e) 10NiO_x-TiO₂, and (f) 10CuO_x-TiO₂.

reaction products were analyzed online by an Agilent GC-MS equipment. 1,2-DCE conversion = $(c_{\text{inlet}} - c_{\text{outlet}})/c_{\text{inlet}} \times 100\%$, where the c_{inlet} and c_{outlet} are the inlet and outlet 1,2-DCE concentrations in the feed stream. HCl and Cl₂ selectivities were determined by bubbling the outlet gas mixture in a sodium hydroxide aqueous solution (12.5 mmol/L) for 0.5 h. The Cl₂ concentration in the bubbled solution was measured via a chemical titration route [15]. The detailed chemical analysis procedures are described in the Supplementary material. 5.0 vol% H₂O was added to the feed stream through a water saturator at 34 °C. 100 ppm HCl provided by a gas cylinder with N₂ as balance was introduced to the reaction system. The balance of carbon throughout the catalytic system was estimated to be 98.5 ± 1.5 %.

3. Results and discussion

3.1. Crystal structure, surface area, and morphology

XRD patterns of the 10MO_x-TiO₂ samples are shown in Fig. 1. The diffraction signals at $2\theta = 25.3^\circ, 36.5^\circ, 37.8^\circ, 38.6^\circ, 48.0^\circ, 53.9^\circ, 55.1^\circ, 62.7^\circ, 68.6^\circ, 70.1^\circ, \text{ and } 75.0^\circ$ could be attributed to the (101), (103), (004), (112), (200), (105), (211), (204), (116), (220), and (215) crystal planes of the anatase-phase TiO₂ (JCPDS PDF# 21-1272) [5]. For the 10MO_x-TiO₂ samples, the feature diffraction peak(s) assignable to the Cr₂O₃ (104), (110), and (300) [16], Mn₂O₃ (104) [17], Fe₂O₃ (104) and (110) [18], NiO (200), or CuO (002) [19] were rather weak, indicating that the MO_x was homogeneously dispersed in the 10MO_x-TiO₂ sample. The ionic radii of the Mⁿ⁺ are smaller than that of Ti⁴⁺, doping of the Mⁿ⁺ into the TiO₂ lattice would give rise to a shrinking in crystal cell of TiO₂. That is to say, the Mⁿ⁺ might be incorporated into the lattice of TiO₂, which contributed to enhancement in interaction between TiO₂ and MO_x and hence improvement in catalytic performance of the 10MO_x-TiO₂ samples for deep oxidation of CVOCs. It should be noted that chromium is not environmentally friendly, and the Cr-based catalysts sometimes suffer from formation of the toxic residues. However, there was no formation of toxic Cr-containing compounds in our Cr₂O₃-TiO₂ samples during the TCE combustion process below 300 °C, since Cr₂O₃ strongly interacted with TiO₂ to generate a Cr₂O₃-TiO₂ solid solution and partial Cr³⁺ ions were incorporated into the lattice of TiO₂.

Table 1
Textural parameters, acidity, and basicity of the samples.

Sample	BET surface area ^a (m ² /g)	D_{TiO_2} ^b (nm)	Average pore size ^c (nm)	Pore volume (cm ³ /g)	Acidity ^d (mmol/g)			Basicity ^e (mmol/g)
					Weak	Strong	Total	
TiO ₂	133	18.8	4.9	0.417	0.019	0.036	0.055	0.12
10CrO _x -TiO ₂	128	18.3	4.8	0.412	0.046	0.172	0.218	0.19
10MnO _x -TiO ₂	114	18.1	5.0	0.416	0.037	0.106	0.143	0.43
10FeO _x -TiO ₂	118	18.3	5.1	0.424	0.043	0.064	0.107	0.20
10NiO _x -TiO ₂	113	18.4	4.9	0.409	0.035	0.043	0.078	0.24
10CuO _x -TiO ₂	120	18.2	5.2	0.414	0.059	0.194	0.253	0.31

^a Surface areas were obtained by the BET method.

^b Data were estimated according to the Scherrer equation using the FWHM of the (101) line of TiO₂.

^c Data were estimated according to the TEM images of the samples.

^d Acidity data were obtained by quantitatively analyzing the desorption peaks in the NH₃-TPD profiles of the samples.

^e Basicity data were obtained by quantitatively analyzing the desorption peaks in the CO₂-TPD profiles of the samples.

Shown in Fig. S1(A) and (B) are the N₂ adsorption-desorption isotherms and pore-size distributions of the TiO₂ and 10MO_x-TiO₂ samples. The samples displayed a IV-typed isotherm with a H2-typed hysteresis loop in the relative pressure range of 0.6–1.0 (Fig. S1(A)), which was indicative of mesopore formation in each sample [16]. Such a deduction was confirmed by appearance of mesopores (3.0–10.0 nm) in the pore-size distributions (Fig. S1(B)). These mesopores were formed due to aggregation of TiO₂ nanoparticles (NPs). Formation of a mesoporous structure could promote adsorption and activation of the CVOCs molecules, hence improving the catalytic performance of a sample. Table 1 summarizes textural parameters of the as-prepared samples, and their BET surface areas, pore volumes, and average pore diameters were in the ranges of 103–133 m²/g, 0.409–0.424 cm³/g, and 4.8–5.2 nm, respectively.

TEM, HAADF-STEM, and elemental mapping characterization methods were used to investigate morphologies, pore structures, and element distributions of the TiO₂ and 10MO_x-TiO₂ samples, as shown in Figs. 2 and 3. The samples contained a number of TiO₂ NPs that were aggregated to form mesopores (Fig. 2), which was consistent with the results of N₂ adsorption-desorption and pore-size distributions. By measuring the sizes of 200 TiO₂ NPs in the TEM images (Fig. 2), we can realize that the sizes of TiO₂ NPs in the TiO₂ and 10MO_x-TiO₂ samples were in the range of 18–25 nm (Table 1 and Figs. 2 and S2). The lattice spacing (d value) of 0.250 nm was in good agreement with that of the TiO₂ (101) plane of the standard sample (Fig. 2j). The HAADF-STEM images and elemental mappings of TiO₂ and 10MO_x-TiO₂ were recorded, as shown in Fig. 3. It can be clearly seen that the M and Ti were well mixed in the samples. Formation of such well mixed 10MO_x-TiO₂ solid solutions suggests existence of a strong synergic action between MO_x and TiO₂ (i.e., formation of a M–O–Ti bond), which could facilitate adsorption and activation of O₂ molecules.

3.2. Low-temperature reducibility, oxygen mobility, surface acidity, and surface basicity

The H₂-TPR technique was used to clarify redox properties of the samples and Fig. 4A illustrates their H₂-TPR profiles. For the TiO₂ sample, two reduction peaks appeared at 295 and 510 °C: The former was assigned to removal of the adsorbed oxygen species on the TiO₂ surface and the latter was associated with reduction of Ti⁴⁺ to Ti³⁺ and lattice oxygen species [4]. After doping of MO_x to TiO₂, there were three or four reduction peaks and their peak temperatures were dependent upon nature of the MO_x. For the MO_x-TiO₂ samples, the reduction peaks below 700 °C mainly originated from reduction of the MO_x species in different phases, in which the one at the lower temperature was ascribable to reduction of the highly distributed MO_x strongly interacting with TiO₂, whereas the one at the higher temperature was attributable to combined reduction of the bulk MO_x and TiO₂. Reduction temperatures of the MO_x species in 10MO_x-TiO₂ were

lower than those in TiO₂, since the strong interaction between TiO₂ and MO_x could improve the mobility of surface lattice oxygen species. Moreover, the chemisorbed oxygen species formed on the sample surface was beneficial for destruction of the CVOCs [20]. We can obtain H₂ consumption of the samples by quantitatively analyzing the reduction peaks in their H₂-TPR profiles, as listed in Table 2. For the sake of better comparison on the low-temperature reducibility, we calculate the initial H₂ consumption rates (less than 25 % oxygen in the first reduction peak of the sample was consumed [21]) of the samples, as illustrated in Fig. 4B. The initial H₂ consumption rate decreased according to 10CrO_x-TiO₂ > 10FeO_x-TiO₂ > 10NiO_x-TiO₂ > 10CuO_x-TiO₂ > 10MnO_x-TiO₂ > TiO₂, which well agreed with their catalytic activity trend.

The O₂-TPD technique was used to measure amounts of the different oxygen species desorbed from the MO_x-TiO₂ and TiO₂ samples (Fig. 5). It is generally established that oxygen is activated via the transformation sequence of O₂ → O₂⁻ → O₂²⁻ → O⁻ → O²⁻ [22]. The O₂⁻, O₂²⁻, and O⁻ species are hard to be differentiated according to their desorption temperatures due to the fact that all of them are desorbed at similar temperatures. Therefore, we could assign the peak at low temperature to desorption of the chemically adsorbed oxygen (O₂⁻, O₂²⁻ or O⁻) species, while the one at high temperature to desorption of the lattice oxygen (O_{latt}) species. There were three oxygen desorption peaks of the TiO₂ sample: The small ones at 155 and 317 °C were ascribable to desorption of the surface adsorbed oxygen species in different coordination environments, while the big one at 630 °C was attributable to desorption of the O_{latt} species in TiO₂. Oxygen desorption of the samples is listed in Table 2. Obviously, oxygen species amount desorbed below 565 °C decreased according to 10CrO_x-TiO₂ (2.44 mmol/g) > 10FeO_x-TiO₂ (1.46 mmol/g) > 10MnO_x-TiO₂ (1.24 mmol/g) > 10NiO_x-TiO₂ (1.14 mmol/g) > 10CuO_x-TiO₂ (1.07 mmol/g) > TiO₂ (0.99 mmol/g), in which the 10CrO_x-TiO₂ sample possessed the highest oxygen desorption amount. Hence, doping of a transition metal oxide could promote desorption of oxygen species on/in the sample.

Fig. 6 illustrates NH₃-TPD profiles of the samples and the corresponding desorption data are listed in Table 1. The peaks below 200 °C were considered as desorption of the physically adsorbed NH₃ at the weak acid sites and the ammonia chemically adsorbed at the moderately strong acid sites in the range of 200–900 °C. However, peak intensity of the desorption from the MO_x-TiO₂ samples became stronger than that from the TiO₂ sample, a result owing to the synergistic action of MO_x and TiO₂. Furthermore, the 10CrO_x-TiO₂ sample had a larger peak area than the TiO₂ sample at high temperatures, suggesting a more amount of the Lewis acid sites on the surface of the former. As compared with the weak acid sites, the strong acid sites were more favorable for deep oxidation of CVOCs, although the weak acid sites were related to CVOCs adsorption [12]. As shown in Table 1, amount of the strong acid sites on the surface of the sample decreased in the sequence of 10CuO_x-TiO₂ (0.194 mmol/g) > 10CrO_x-TiO₂ (0.172 mmol/

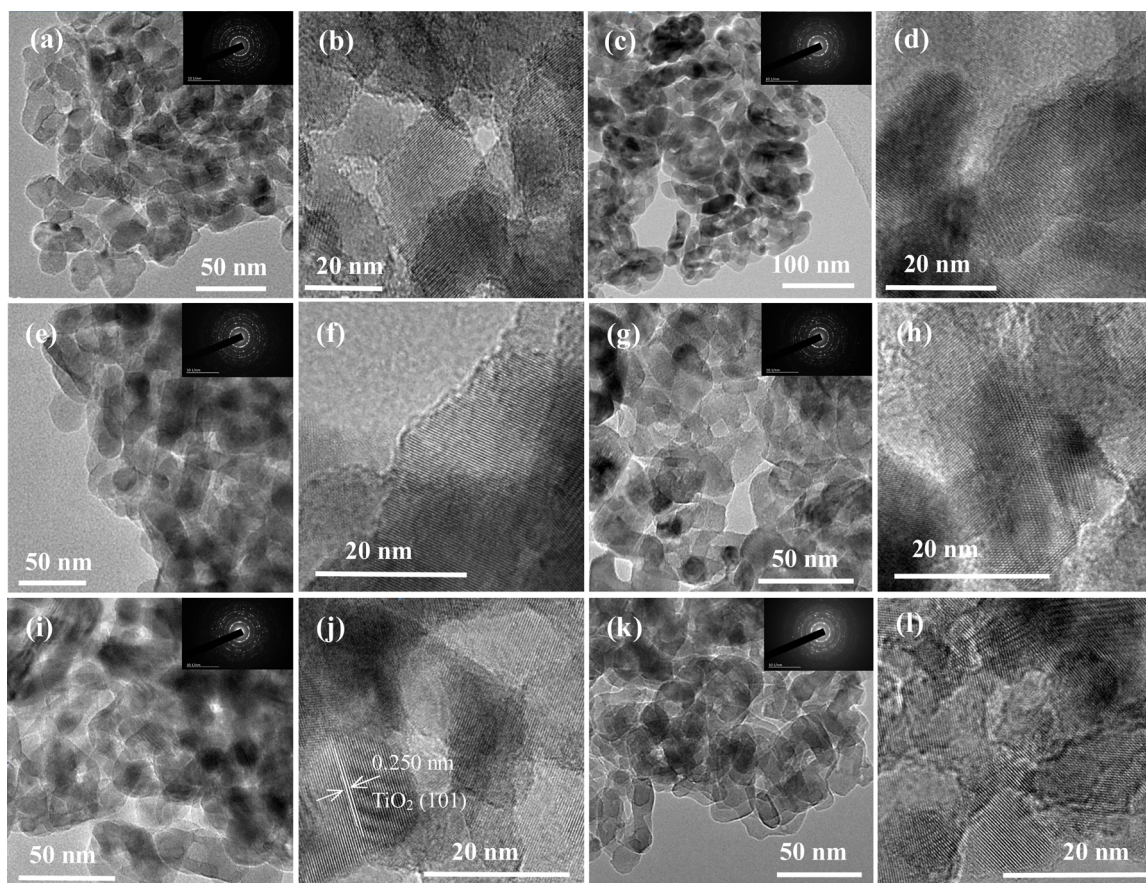


Fig. 2. TEM images and SAED patterns (insets) of (a, b) TiO_2 , (c, d) $10\text{CrO}_x\text{-TiO}_2$, (e, f) $10\text{MnO}_x\text{-TiO}_2$, (g, h) $10\text{FeO}_x\text{-TiO}_2$, (i, j) $10\text{NiO}_x\text{-TiO}_2$, and (k, l) $10\text{CuO}_x\text{-TiO}_2$.

$g) > 10\text{MnO}_x\text{-TiO}_2$ (0.106 mmol/g) $> 10\text{FeO}_x\text{-TiO}_2$ (0.064 mmol/g) $> 10\text{NiO}_x\text{-TiO}_2$ (0.043 mmol/g) $> \text{TiO}_2$ (0.036 mmol/g), which was inconsistent with their catalytic activity order, demonstrating that the surface acidity was not the only factor determining catalytic activity of the sample.

Shown in Fig. 7 are CO_2 -TPD profiles of the $\text{MO}_x\text{-TiO}_2$ and TiO_2 samples. There was one peak at 70–160 °C (corresponding to the weak basic sites (surface hydroxyl groups) in the CO_2 -TPD profiles), while the other peaks were associated with the medium-strength basicity (oxygen ions) [7,23]. Obviously, due to doping of the transition metal oxide to anatase TiO_2 nanocrystal, the basicity of $10\text{MO}_x\text{-TiO}_2$ was significantly enhanced in strength and amount as compared with that of TiO_2 , which was an advantageous property for CO_2 adsorption. There have been some researchers to investigate the roles of acidic sites in catalyzing the oxidation of CVOCs. For example, Wang et al. [24] found that the Cr species in CoCr_2O_4 provided surface acidic sites for chemisorption of CH_2Cl_2 (DCM). Yang et al. [11] thought that the CrO_x in $4\text{Ce}1\text{Cr}$ exhibited a good promotion effect for both TCE and CB removal due to the strong interaction between CrO_x and CeO_2 and the formation of Cr^{6+} species with a high oxidizing ability. Wang and coworkers [25] found that the Ti species in $\text{Ce}_{1-x}\text{Ti}_x\text{O}_2$ promoted formation of the strong acidic sites due to the electronic unbalance induced by the change in length of Ce–O and Ti–O bonds; additionally, TiO_2 is acidic solid, and $\text{Ce}^{3+}/\text{Ce}^{4+}$ and $\text{Ti}^{3+}/\text{Ti}^{4+}$ species contributed to the Lewis acid sites. The C–Cl dissociation on the Lewis acidic sites led to formation of chlorinated methoxy during the oxidation of DCM [7]. Shi et al. [14] pointed out that DCE firstly adsorbed on the Lewis acid sites of the $\text{CeO}_2\text{-TiO}_2$ catalysts to form $\text{C}_2\text{H}_3\text{Cl}$ through dehydrochlorination, and then the $\text{C}_2\text{H}_3\text{Cl}$ interacted with the surface hydroxy to form + $\text{C}_2\text{H}_3\text{Cl}$ carbocation, and the catalysts with larger amounts of acid sites were

suitable for adsorption, activation and deep oxidation of DCE. Although pure TiO_2 possessed a small amount of acid sites, introduction of Ce to TiO_2 noticeably increased the amount of acid sites (especially the Lewis acid sites). Therefore, the interaction between CeO_2 and TiO_2 enhanced the acid strength and promoted the dechlorination of DCE. Tian et al. [26] claimed that 1,2-DCE was firstly adsorbed on the Lewis acid sites, resulting in formation of the main byproducts by dehydrochlorination. The weak acid sites at low temperature was associated with desorption of ammonia from the Lewis acid sites, whereas the strong acid sites at high temperature was related to desorption of ammonia from the Brønsted acid sites. Over the $10\text{CrO}_x\text{-TiO}_2$ sample, the C–Cl bonds in 1,2-DCE could be dissociated more readily due to presence of more amounts of the Lewis acid sites ($\text{Cr}^{6+/4+}$ and $\text{Ti}^{4+/3+}$) as well as the Cr–O–Ti interfaces [7]. The higher oxidation state of Cr ions, electrophilicity of CrO_x species, and stronger $\text{CrO}_x\text{-TiO}_2$ interaction (as compared with the isolated TiO_2) might be responsible for the high catalytic activity of $10\text{CrO}_x\text{-TiO}_2$. Furthermore, concurrent adsorption and dissociation of the C–Cl bonds on $10\text{CrO}_x\text{-TiO}_2$ were more efficient because the absence of abundant basic sites could enhance selective oxidation of 1,2-DCE.

3.3. Surface property

To further obtain the information of surface compositions and metal chemical states, we performed XPS characterization of the samples, and the XPS spectra are illustrated in Figs. 8, S3, and S4. C 1s peak at 284.6 eV was used to calibrate binding energies (BEs) of the other elements. The asymmetric O 1s signal was decomposed into three components at BE = 529.6, 531.5, and 532.8 eV (Fig. 8A), which were assigned to the O_{latt} , O_{ads} , and carbonate or adsorbed water species [27], respectively.

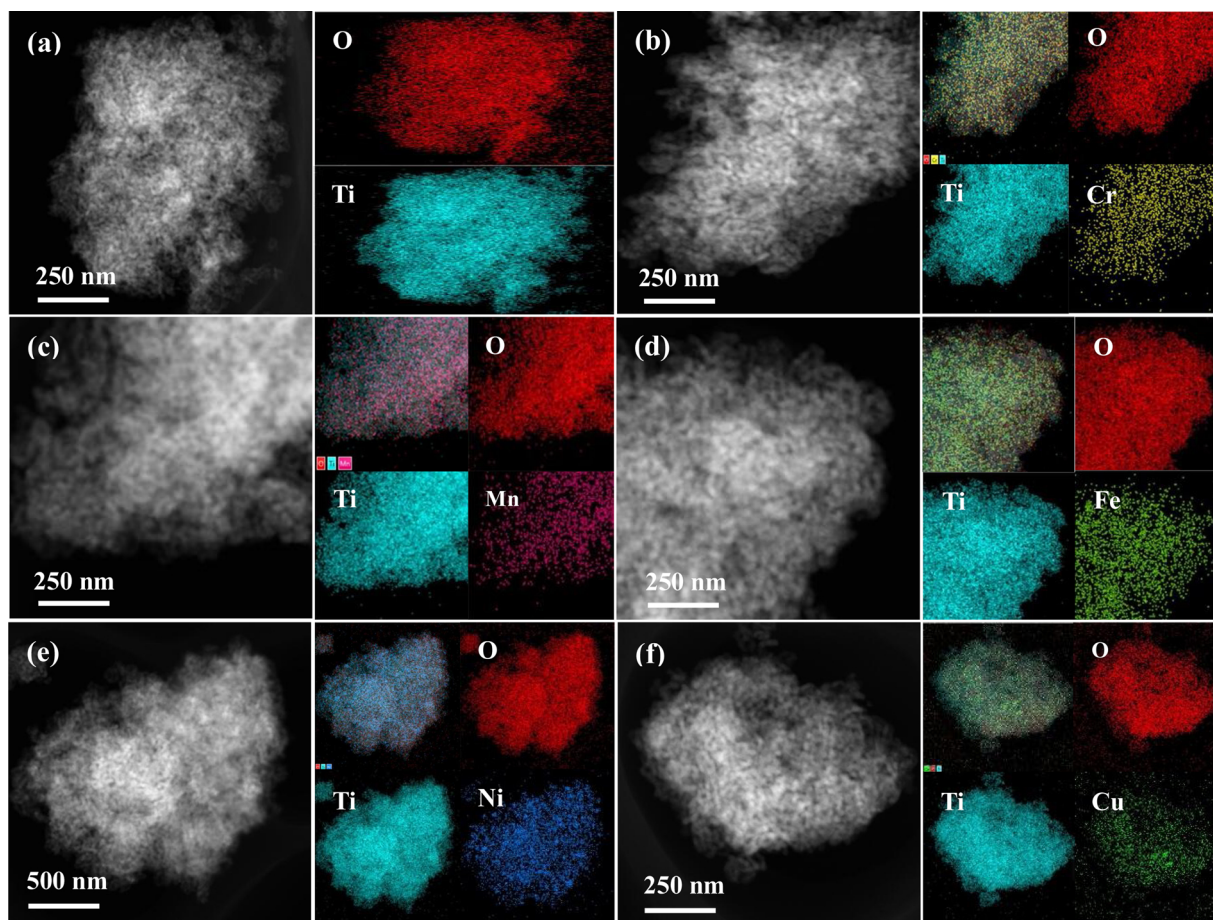


Fig. 3. HAADF-STEM images and elemental mappings of (a) TiO_2 , (b) $10\text{CrO}_x\text{-TiO}_2$, (c) $10\text{MnO}_x\text{-TiO}_2$, (d) $10\text{FeO}_x\text{-TiO}_2$, (e) $10\text{NiO}_x\text{-TiO}_2$, and (f) $10\text{CuO}_x\text{-TiO}_2$.

It is well known that the higher surface oxygen vacancy density of a catalyst favors the activation adsorption of O_2 molecules to the electrophilic O_{ads} species that can play an important role in deep oxidation of CVOs. The $\text{O}_{\text{ads}}/\text{O}_{\text{latt}}$ molar ratio (Table 2) decreased in the order of $10\text{CrO}_x\text{-TiO}_2$ (0.32) > $10\text{FeO}_x\text{-TiO}_2$ (0.28) > $10\text{NiO}_x\text{-TiO}_2$ (0.24) > $10\text{CuO}_x\text{-TiO}_2$ (0.22) > $10\text{MnO}_x\text{-TiO}_2$ (0.21) > TiO_2 (0.16), in good consistency with the changing trend in activity (shown below). In the Ti 2p XPS spectra of the samples (Fig. S4), there were the Ti $2p_{1/2}$ and Ti $2p_{3/2}$ final states of the Ti^{4+} species at BE = 464.2 and 458.6 eV, respectively. The Cr $2p_{3/2}$ XPS spectrum of the sample was decomposed

into two components at BE = 576.4 and 578.9 eV (Fig. 8B), attributable to the surface Cr^{3+} and Cr^{6+} species [28,29], respectively. The $\text{Cr}^{6+}/\text{Cr}^{3+}$ molar ratio on the sample was 11.0 (Table 2). According to the literature [30], Cr^{6+} species exhibited a strong oxidizing ability and presence of the Cr^{6+} species was beneficial for deep oxidation of CVOs. The Cu $2p_{3/2}$ XPS spectrum of $10\text{CuO}_x\text{-TiO}_2$ was divided into two strong peaks at BE = 932.5 eV (the surface Cu^0 species) and 934.5 eV (the surface Cu^{2+} species), and a shake-up satellite at BE = 942.0 eV was indicative of presence of Cu^{2+} [31]. The Ni $2p_{3/2}$ XPS spectrum contained two principal peaks at BE = 852.7 and 855.5 eV,

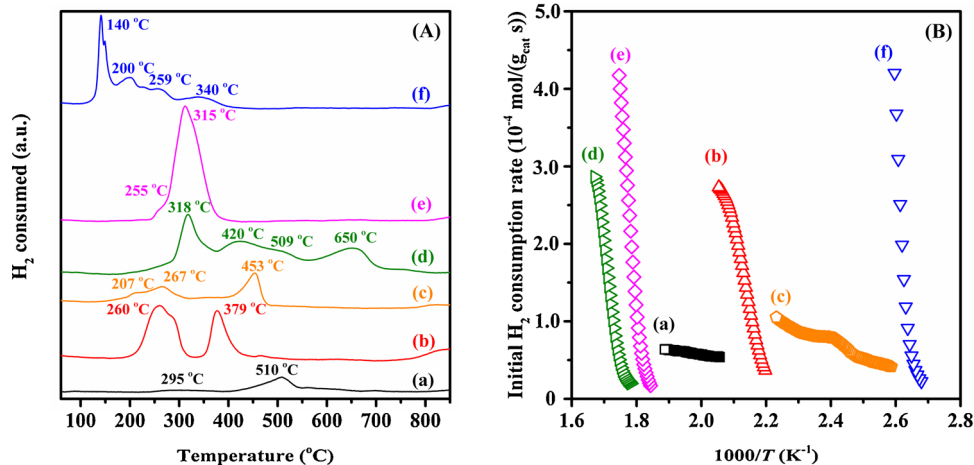


Fig. 4. (A) H_2 -TPR profiles and (B) initial H_2 consumption rate versus inverse temperature of (a) TiO_2 , (b) $10\text{CrO}_x\text{-TiO}_2$, (c) $10\text{MnO}_x\text{-TiO}_2$, (d) $10\text{FeO}_x\text{-TiO}_2$, (e) $10\text{NiO}_x\text{-TiO}_2$, and (f) $10\text{CuO}_x\text{-TiO}_2$.

Table 2
Surface element compositions, O₂ desorption, and H₂ consumption of the samples.

Sample	Surface element composition ^a		O ₂ desorption ^b (mmol/g)				H ₂ consumption ^c (mmol/g)		
	Molar ratio of different metal ions	O _{ads} /O _{latt} molar ratio	100–225 °C	225–565 °C	565–900 °C	Total	< 400 °C	≥ 400 °C	Total
TiO ₂	–	0.16	0.10	0.89	0.15	1.14	0.24	0.89	1.13
10CrO _x -TiO ₂	1.32 (Cr ⁶⁺ /Cr ³⁺)	0.32	1.21	1.23	0.13	2.57	2.17	0.34	2.51
10MnO _x -TiO ₂	1.66 (Mn ³⁺ /Mn ²⁺)	0.21	0.08	1.16	1.29	2.53	0.85	0.57	1.42
10FeO _x -TiO ₂	0.84 (Fe ³⁺ /Fe ²⁺)	0.28	0.11	1.35	1.03	2.49	1.21	1.24	2.45
10NiO _x -TiO ₂	2.61 (Ni ²⁺ /Ni ⁰)	0.24	0.06	1.08	1.09	2.23	2.28	–	2.28
10CuO _x -TiO ₂	1.85 (Cu ²⁺ /Cu ⁰)	0.22	0.05	1.02	1.65	2.72	2.04	–	2.04

^a Data were estimated by quantitatively analyzing the peaks in the XPS spectra of the samples.

^b Data were calculated by quantitatively analyzing the desorption peaks in the O₂-TPD profiles of the samples.

^c Data were obtained by quantitatively analyzing the reduction peaks in the H₂-TPR profiles of the samples.

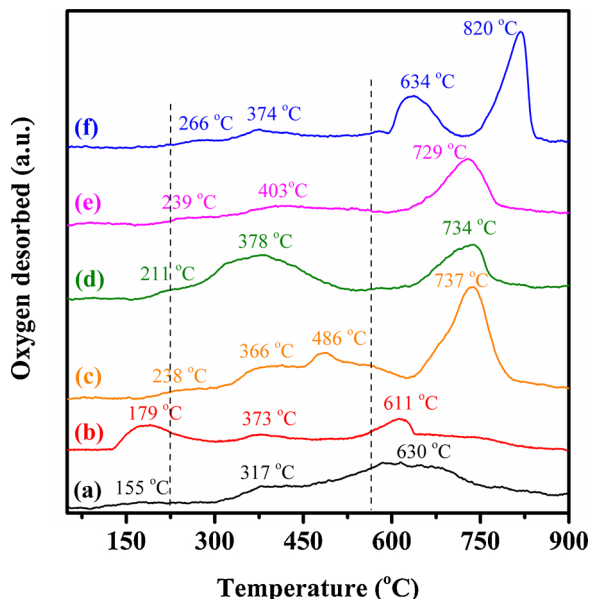


Fig. 5. O₂-TPD profiles of (a) TiO₂, (b) 10CrO_x-TiO₂, (c) 10MnO_x-TiO₂, (d) 10FeO_x-TiO₂, (e) 10NiO_x-TiO₂, and (f) 10CuO_x-TiO₂.

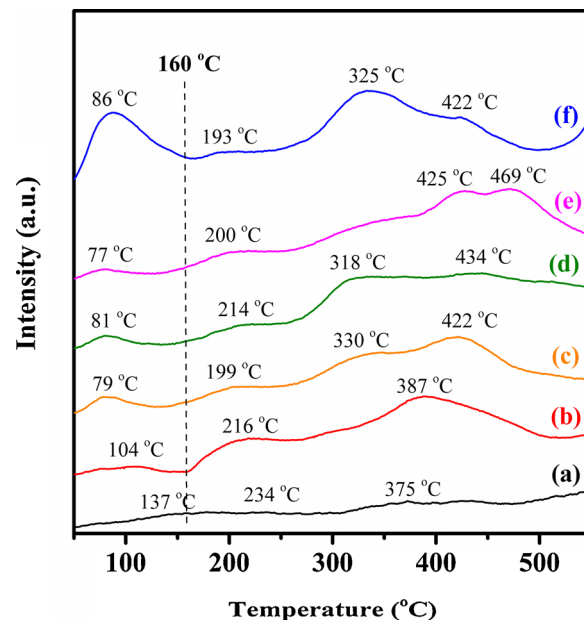


Fig. 7. CO₂-TPD profiles of (a) TiO₂, (b) 10CrO_x-TiO₂, (c) 10MnO_x-TiO₂, (d) 10FeO_x-TiO₂, (e) 10NiO_x-TiO₂, and (f) 10CuO_x-TiO₂.

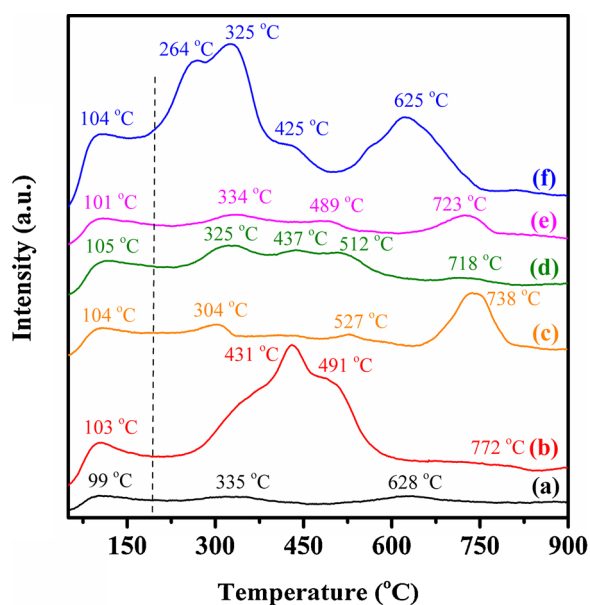


Fig. 6. NH₃-TPD profiles of (a) TiO₂, (b) 10CrO_x-TiO₂, (c) 10MnO_x-TiO₂, (d) 10FeO_x-TiO₂, (e) 10NiO_x-TiO₂, and (f) 10CuO_x-TiO₂.

which were attributed to the surface metallic Ni⁰ and Ni²⁺ species, respectively, while a satellite peak of Ni 2p_{3/2} occurred at BE = 860.8 eV [32]. The asymmetrical Mn 2p_{3/2} spectrum was decomposed into three components at BE = 640.3, 641.7, and 644.7 eV: The former two corresponded to the surface Mn²⁺ and Mn³⁺ species, while the last one was a satellite of Mn²⁺ species [33]. The asymmetrical Fe 2p_{3/2} signal was composed of three components at BE = 710.5, 712.5, and 717.8 eV, belonging to the surface Fe²⁺ and Fe³⁺ species and the satellite of Fe²⁺ species [34], respectively. The surface Cr⁶⁺/Cr³⁺, Mn³⁺/Mn²⁺, Fe³⁺/Fe²⁺, Ni²⁺/Ni⁰, and Cu²⁺/Cu⁰ molar ratios on the CrO_x, MnO_x, FeO_x, NiO_x, and CuO_x-doped TiO₂ samples were 1.32, 1.66, 0.84, 2.61, and 1.85, respectively. According to the results of O_{ads}/O_{latt} molar ratio calculated by quantitatively analyzing the peaks of the O 1s XPS spectra and catalytic activities of the samples, one can realize that the sequence in O_{ads}/O_{latt} molar ratio was in basic agreement with that in catalytic activity of these samples. It was reported that the surface adsorbed oxygen species favored the deep oxidation of CVOCs, and the Cr⁶⁺ species were much more active than the Cr³⁺ species for the oxidation of CH₂Cl₂ [35] and 1,2-DCE [12]. Therefore, the 10CrO_x-TiO₂ sample with high O_{ads}/O_{latt} and Cr⁶⁺/Cr³⁺ molar ratios exhibited the best catalytic activity for the oxidation of 1,2-DCE (as shown below). Partial Cr³⁺ ions were incorporated into the lattice of TiO₂, resulting in an increase in oxygen vacancy density and hence a rise in O_{ads} concentration. The interaction between Cr₂O₃ and TiO₂ generated a Cr₂O₃-TiO₂ solid solution, in which a strong interaction

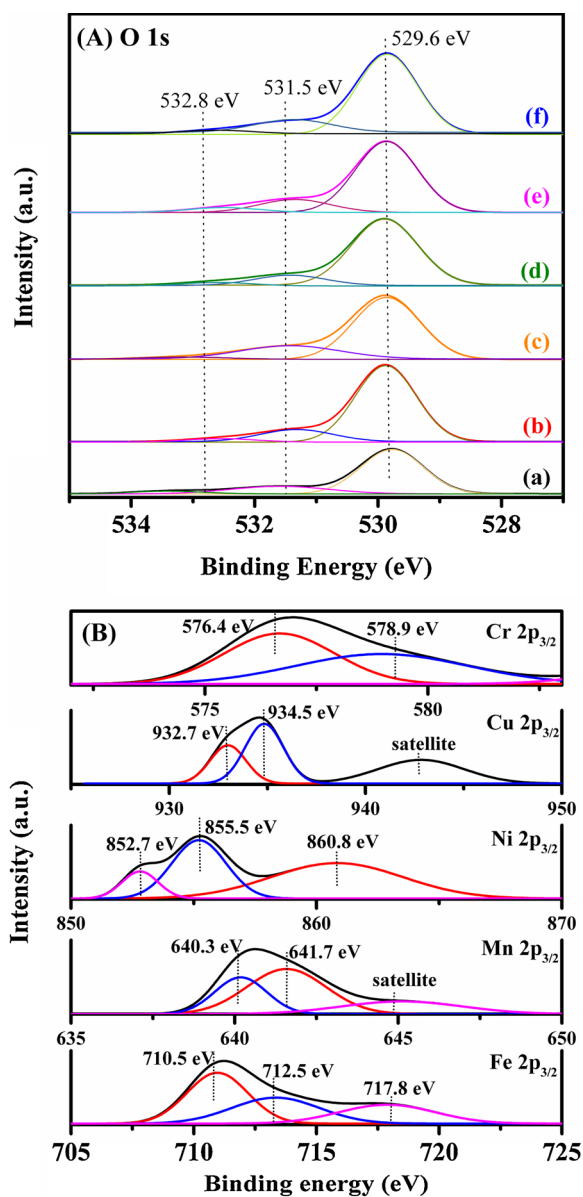


Fig. 8. (A) O 1s, (B) Cr 2p_{3/2}, Mn 2p_{3/2}, Fe 2p_{3/2}, Ni 2p_{3/2}, and Cu 2p_{3/2} XPS spectra of (a) TiO₂, (b) 10CrO_x-TiO₂, (c) 10MnO_x-TiO₂, (d) 10FeO_x-TiO₂, (e) 10NiO_x-TiO₂, and (f) 10CuO_x-TiO₂.

would exist between CrO_x and TiO₂. Furthermore, doping of chromia increased amount of the strong acid sites. Therefore, the O_{ads} species concentration, low-temperature reducibility, and strong interaction between Cr₂O₃ and TiO₂, and strong acidity were the factors influencing catalytic performance of the 10Cr₂O₃-TiO₂ sample for 1,2-DCE combustion.

3.4. Catalytic performance and selectivity

Catalytic activities of the 10MO_x-TiO₂ and TiO₂ samples were measured for 1,2-DCE oxidation, as shown in Fig. 9. In order to better compare catalytic activities of these samples, we use the reaction temperatures $T_{10\%}$, $T_{50\%}$, and $T_{90\%}$ (corresponding to 1,2-DCE conversion = 10, 50, and 90 %), as listed in Table 3. The pure TiO₂ sample showed a poor catalytic activity, but the activity was significantly enhanced with the doping of MO_x (Fig. 9A), and 10CrO_x-TiO₂ presented the highest catalytic activity. The sequence in catalytic activity for 1,2-DCE destruction at SV = 40,000 mL/(g h) was 10CrO_x-TiO₂

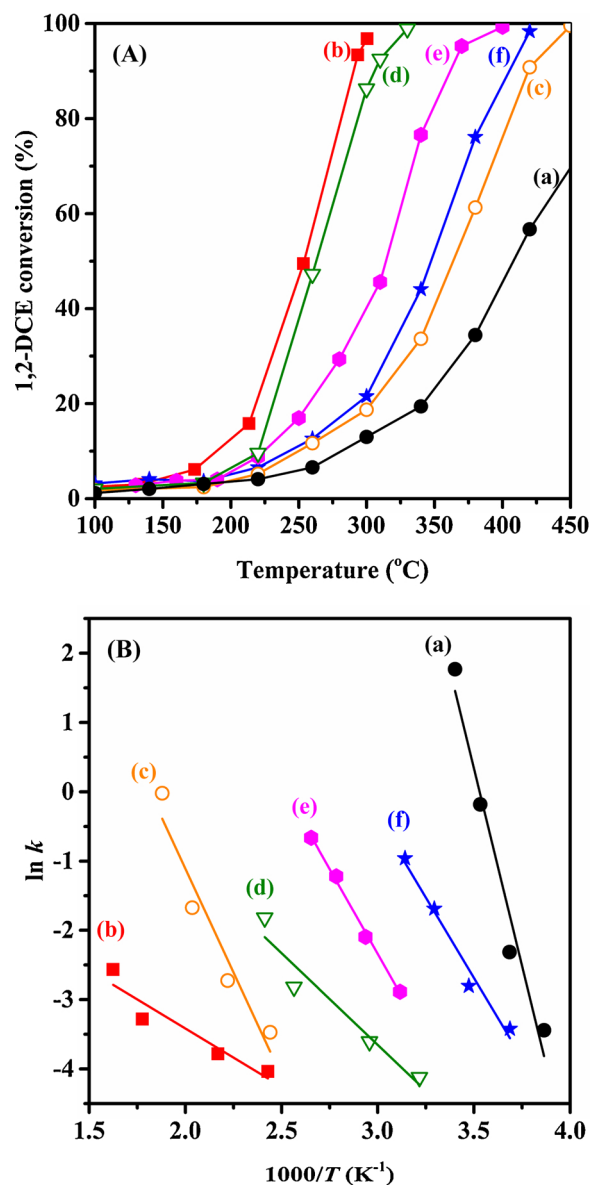


Fig. 9. (A) 1,2-DCE conversion as a function of reaction temperature and (B) $\ln k$ versus inverse temperature over (a) TiO₂, (b) 10CrO_x-TiO₂, (c) 10MnO_x-TiO₂, (d) 10FeO_x-TiO₂, (e) 10NiO_x-TiO₂, and (f) 10CuO_x-TiO₂ at SV = 40,000 mL/(g h).

Table 3

Catalytic activities, HCl selectivities (S_{HCl}), reaction rates, and apparent activation energies (E_a) over the samples for 1,2-DCE oxidation at SV = 40,000 mL/(g h).

Sample	Catalytic activity for 1,2-DCE oxidation				Reaction rate at 260 °C (mol/(g _{cat} s))	E_a (kJ/mol)
	$T_{10\%}$ (°C)	$T_{50\%}$ (°C)	$T_{90\%}$ (°C)	S_{HCl}^a		
TiO ₂	274	410	–	37.6	2.99×10^{-8}	89
10CrO _x -TiO ₂	186	255	284	89.6	2.35×10^{-7}	35
10MnO _x -TiO ₂	254	372	425	73.8	5.29×10^{-8}	69
10FeO _x -TiO ₂	223	261	305	83.1	2.14×10^{-7}	38
10NiO _x -TiO ₂	225	320	363	73.6	7.70×10^{-8}	53
10CuO _x -TiO ₂	238	359	402	79.5	5.73×10^{-8}	61

^a $S_{\text{HCl}} = [\text{HCl}]/([\text{HCl}] + 2[\text{Cl}_2])$ in 1,2-DCE oxidation at 450 °C.

($T_{90\%} = 284\text{ }^{\circ}\text{C}$) > 10FeO_x-TiO₂ ($T_{90\%} = 305\text{ }^{\circ}\text{C}$) > 10NiO_x-TiO₂
 ($T_{90\%} = 363\text{ }^{\circ}\text{C}$) > 10CuO_x-TiO₂ ($T_{90\%} = 402\text{ }^{\circ}\text{C}$) > 10MnO_x-TiO₂
 ($T_{90\%} = 425\text{ }^{\circ}\text{C}$).

We calculate the 1,2-DCB reaction rates (normalized by per gram of noble metal) achieved over the samples (Table 3). Apparently, the reaction rate at 260 °C decreased in the order of 10CrO_x-TiO₂ (2.35×10^{-7} mol/(g_{cat} s)) > 10FeO_x-TiO₂ (2.14×10^{-7} mol/(g_{cat} s)) > 10NiO_x-TiO₂ (7.7×10^{-8} mol/(g_{cat} s)) > 10CuO_x-TiO₂ (5.73×10^{-8} mol/(g_{cat} s)) > 10MnO_x-TiO₂ (5.29×10^{-8} mol/(g_{cat} s)) > TiO₂ (2.99×10^{-8} mol/(g_{cat} s)). The oxidation of CVOCs over CeO₂-TiO₂ [25] obeyed a reaction mechanism: first-order toward CVOC concentration and zero-order toward O₂ concentration. We can reasonably suppose that 1,2-DCE oxidation in an excessive oxygen atmosphere obey a first-order reaction mechanism with respect to 1,2-DCE concentration (*c*). The reaction rate (*r* (mol/s)) equation is: $r = -k c = (-A \exp(-E_a/RT)) c$, where *k*, *A*, and *E_a* are the rate constant (s⁻¹), pre-exponential factor, and apparent activation energy (kJ/mol), respectively. A lower *E_a* means a better catalytic activity of a sample. Based on the Arrhenius plots under the conditions of 1,2-DCE conversions < 20 % and SV = 40,000 mL/(g h) (Fig. 9B), we can obtain the kinetic parameters (Table 3). The *E_a* increased in the order of 10CrO_x-TiO₂ (35 kJ/mol) < 10FeO_x-TiO₂ (38 kJ/mol) < 10NiO_x-TiO₂ (53 kJ/mol) < 10CuO_x-TiO₂ (61 kJ/mol) < 10MnO_x-TiO₂ (69 kJ/mol) < TiO₂ (89 kJ/mol).

Fig. 10 shows concentrations of the main by-products (C₂H₃Cl, CO, and CO₂) generated during the 1,2-DCE oxidation over the samples at

SV = 40,000 mL/(g h). C₂H₃Cl concentrations over 10MO_x-TiO₂ (the maximum C₂H₃Cl concentration at 160–250 °C was < 5 ppm) were much lower than that over pure TiO₂ (Fig. 10A), which was principally due to the high activity and synergistic effect of MO_x and TiO₂ or reduction of the acid sites of the MO_x-doped samples. It has been reported that C₂H₃Cl was generated through dehydrochlorination of 1,2-DCE at the Lewis acid sites [36]. HCl and Cl₂ were the final chlorinated products when 1,2-DCE and C₂H₃Cl were completely oxidized. As it is well known, HCl is easier to be treated and less toxic than Cl₂. Therefore, a high HCl selectivity means that the polychlorinated byproducts could be avoided in the oxidation of 1,2-DCE. HCl selectivities (*S_{HCl}* = [HCl]/([HCl] + [Cl₂])) over all of the samples under the steady-state conditions were calculated. It can be clearly seen from the data in Table 3 that all of the samples exhibited a high HCl selectivity. Moreover, CO and CO₂ were the carbon-containing products, and their concentrations increased obviously with a rise in temperature (Fig. 10B and C). CO concentration in the products over 10CuO_x-TiO₂ or 10FeO_x-TiO₂ was higher than those over the other samples. At 400–580 °C, CO₂ concentrations over 10MO_x-TiO₂ were higher than that over TiO₂, which was possibly due to the facts that TiO₂ possessed a weaker deep oxidation ability and doping of MO_x to TiO₂ enhanced adsorption of 1,2-DCE and oxygen species as well as oxygen mobility. The doping of a transition metal oxide could increase redox properties of the sample, which was favorable for the oxidation of 1,2-DCE and elimination of the Cl species from the surface of the sample, whereas the strong acid sites possibly promoted the breaking of the C–Cl bonds. MO_x doping could

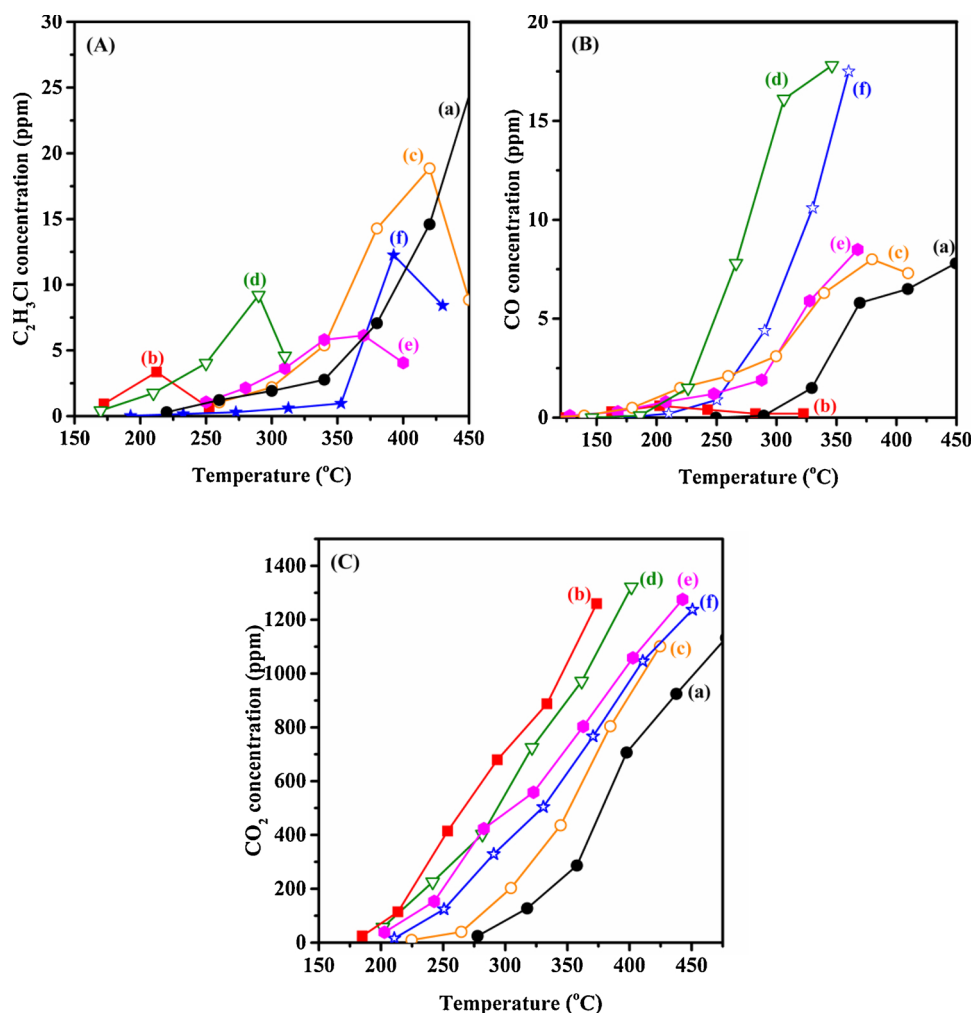


Fig. 10. (A–C) Product distributions of 1,2-DCE oxidation at SV = 40,000 mL/(g h) over (a) TiO₂, (b) 10CrO_x-TiO₂, (c) 10MnO_x-TiO₂, (d) 10FeO_x-TiO₂, (e) 10NiO_x-TiO₂, and (f) 10CuO_x-TiO₂.

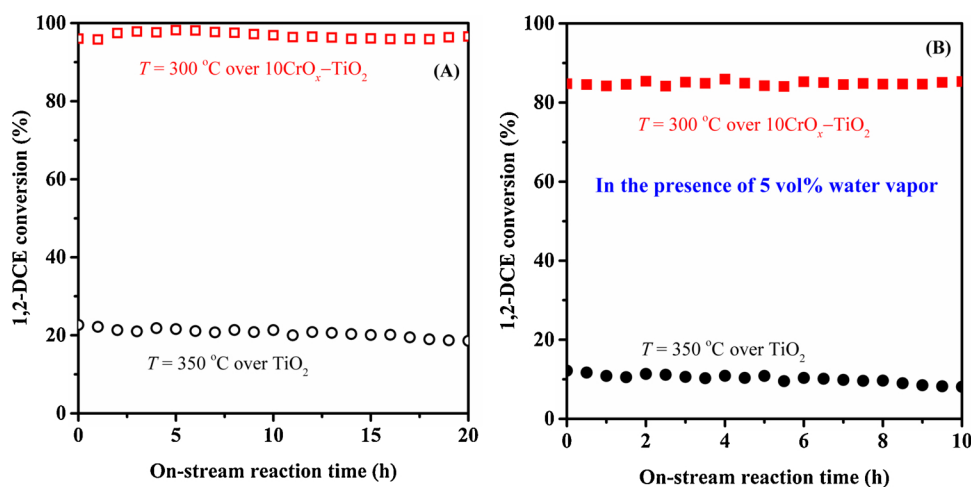


Fig. 11. 1,2-DCE conversion as a function of on-stream reaction time over TiO_2 and $10\text{CrO}_x\text{-TiO}_2$ in the (A) absence and (B) presence of 5 vol% water vapor at $\text{SV} = 40,000 \text{ mL}/(\text{g h})$.

also promote secondary catalytic decomposition of the chlorine-containing by-products.

Doping of MO_x to TiO_2 could modify the chemical environment via generation of oxygen vacancies and prohibit adsorption of the Cl species. The O_{ads} species were formed at oxygen vacancies, and a more amount of oxygen vacancies could give rise to a more amount of O_{ads} species. Furthermore, the MO_x with there were variable oxidation states of M in MO_x , and MO_x doping could improve the reducibility of TiO_2 . Hence, addition of MO_x to TiO_2 could improve the reducibility of TiO_2 and increase the surface O_{ads} species. The catalytically active sites in $\text{MO}_x\text{-TiO}_2$ were the MO_x with good redox properties and O_{ads} species formed at oxygen vacancies. As stated previously, part of the Cr^{3+} ions were incorporated into the lattice of TiO_2 , generating oxygen vacancies and increasing the active O_{ads} species concentration; moreover, the presence of Cr^{6+} species with a strong oxidizing ability was beneficial for the deep oxidation of CVOCs.

3.5. Catalytic stability and effects of H_2O and HCl on activity

Fig. 11A and B presents catalytic stability of TiO_2 and $10\text{CrO}_x\text{-TiO}_2$ and their hydrothermal stability in the presence of 5 vol% water vapor for 1,2-DCE oxidation at $\text{SV} = 40,000 \text{ mL}/(\text{g h})$ and different temperatures, respectively. No significant decreases in activity were observed after 20 h of on-stream reaction (Fig. 11A). As can be seen from Fig. 11 B, 1,2-DCE conversion over $10\text{CrO}_x\text{-TiO}_2$ did not alter considerably, whereas that over TiO_2 decreased gradually. The good thermal and hydrothermal stability of $10\text{CrO}_x\text{-TiO}_2$ was associated with presence of the strong $\text{CrO}_x\text{-TiO}_2$ interaction. We also examined the morphology change of the used $10\text{CrO}_x\text{-TiO}_2$ sample, and its TEM image and particle-size distribution is shown in Fig. S5 of the Supplementary material. Obviously, there was no apparent growth in particle size (18.5 nm) of TiO_2 in the used sample, as compared with that (18.3 nm) of TiO_2 in the fresh sample.

The final products are CO, CO_2 , H_2O , HCl, and Cl_2 in the complete oxidation of 1,2-DCE. Since water is one of the products in 1,2-DCE oxidation, it is hence important to probe the influence of water vapor on activity of a catalyst. We measured catalytic activities at $\text{SV} = 40,000 \text{ mL}/(\text{g h})$ and different temperatures of the TiO_2 and $10\text{CrO}_x\text{-TiO}_2$ samples in the presence of 5.0 vol% water vapor in the feed stream (Fig. 12A). When 5 vol% water vapor was introduced to the reaction system, the $T_{90\%}$ over $10\text{CrO}_x\text{-TiO}_2$ decreased only slightly (by 6 °C), but that over pure TiO_2 went down considerably (by more than 50 °C). Therefore, the $10\text{CrO}_x\text{-TiO}_2$ sample exhibited much better water-resistant performance than the pure TiO_2 sample. Partial deactivation of the samples was owing to competitive adsorption of H_2O ,

1,2-DCE, and O_2 on the active sites. Fig. 12B shows catalytic activity at 290 °C and $\text{SV} = 40,000 \text{ mL}/(\text{g h})$ of the $10\text{CrO}_x\text{-TiO}_2$ sample in the absence and presence of 100 ppm HCl in the feed stream. Only a small drop in activity was seen after 100 ppm HCl introduction. Most of the CrO_x in $10\text{CrO}_x\text{-TiO}_2$ were highly dispersed in the solid solution, which effectively prohibited adsorption of HCl and Cl^- at higher temperatures on the catalyst surface and hence retaining the activity.

3.6. Surface 1,2-DCE reaction

In order to clarify the 1,2-DCE oxidation behaviors over TiO_2 and $10\text{CrO}_x\text{-TiO}_2$, we carried out the TPSR experiments, in which evolution of the possible intermediates and products was online monitored by a mass spectrometer. The $10\text{CrO}_x\text{-TiO}_2$ sample showed a more obvious 1,2-DCE desorption peak as compared with the pure TiO_2 sample, proving that $10\text{CrO}_x\text{-TiO}_2$ possessed a larger 1,2-DCE adsorption capacity (Fig. 13a). The temperatures for $\text{C}_2\text{H}_3\text{Cl}$ formation over pure TiO_2 were higher than those over $10\text{CrO}_x\text{-TiO}_2$ (Fig. 13b), indicating that $\text{C}_2\text{H}_3\text{Cl}$ formation during the oxidation of 1,2-DCE was inhibited to a certain extent after the doping of CrO_x . Over the two samples, HCl was the main chlorinated product of 1,2-DCE oxidation under the adopted conditions (Fig. 13c and d), and the increased Cl_2 amount over TiO_2 at high temperatures was contributed by the Deacon reaction ($\text{HCl} + \text{O}_2 \rightarrow \text{Cl}_2 + \text{H}_2\text{O}$) and re-combination of dissociatively adsorbed Cl species [5]. CO_2 was formed over $10\text{CrO}_x\text{-TiO}_2$ at lower temperatures and its intensity was higher than that over pure TiO_2 , which was in consistency with their catalytic activity trend. However, the change in CO concentration was the opposite. CO was detected over pure TiO_2 and $10\text{CrO}_x\text{-TiO}_2$, and intensity of the CO peak was higher over TiO_2 than that over $10\text{CrO}_x\text{-TiO}_2$ (Fig. 13e and f), in good agreement with a deep oxidation ability of the former weaker than that of the latter.

3.7. Reaction pathway

In order to study the 1,2-DCE oxidation mechanisms, we measured the in situ DRIFTS spectra of the TiO_2 and $10\text{CrO}_x\text{-TiO}_2$ samples for 1,2-DCE oxidation at 100–500 °C (Fig. 14). The negative bands at 3628, 3670, and 3691 cm^{-1} were assigned to the OH vibration mode, and the ones at 2975, 2932, and 2878 cm^{-1} were attributed to the C–H stretching mode, and their intensity was changed with the rise in reaction temperature [37]. The bands at 1426, 1180, 1290, and 1309 cm^{-1} were related to the $\delta(\text{CH}_2\text{Cl})$, $\nu(\text{CH})$, $\delta(\text{CCH})$ and $\nu(\text{CC})/\delta(\text{CCH})$ in 1,2-DCE [10]. The bands at 1426 and 950 cm^{-1} were assigned to deformation of the $-\text{CH}_2-$ and $-\text{CH}-$ groups. The band at

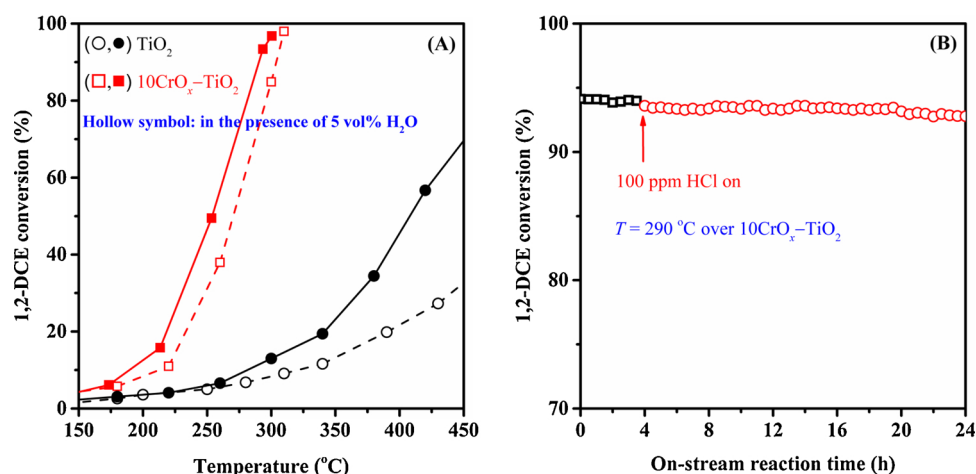


Fig. 12. Effects of (A) 5 vol% water vapor and (B) 100 ppm HCl on catalytic activity of TiO₂ and/or 10CrO_x-TiO₂ at SV = 40,000 mL/(g h).

890 cm⁻¹ was ascribed to stretching vibration of the C–Cl bonds [38]. Intensity of the bands at 1690–1750 cm⁻¹ (due to carbonyl group of aldehyde) increased, signifying that the aldehyde species was one of intermediates during the 1,2-DCE oxidation process. With a rise in temperature, intensity of the 1,2-DCE bands decreased and gradually disappeared, and some new bands appeared at the same time. The bands corresponding to C₂H₃Cl (such as $\rho(\text{CH})$ at 1290 cm⁻¹ and $\nu(\text{C}=\text{C})$ at 1545 cm⁻¹) were recorded. It can be verified that when reaction temperature rose, amount of C₂H₃Cl formed during 1,2-DCE oxidation was increased [10]. The band at 1050 cm⁻¹ was owing to oxygen–oxygen stretching vibration of the O_{ads} species and the band at 1020 cm⁻¹ originated from the HCOO⁻ species [27]. The O₂⁻ and HCOO⁻ species appeared with the rise in temperature, and amount of the O₂⁻ and/or HCOO⁻ species on the 10CrO_x-TiO₂ sample was much more than that on the TiO₂ sample. The results were in good agreement with those of the O₂-TPD characterization. The hydrochloric acid peaks

generated were difficult to be observed due to the weak adsorption, but the TPSR results confirmed its formation.

Based on the results of DRIFTS and TPSR characterization as well as those reported in the literature, we thought that 1,2-DCE oxidation over TiO₂ and 10CrO_x-TiO₂ might take place according to the Mars-van Krevelen mechanism, in which O₂ molecules were activated by picking up the electrons from 10MO_x-TiO₂ to generate the O_{ads} species [39]. 1,2-DCE was oxidized through the redox process of the adsorbed 1,2-DCE and adsorbed oxygen species and/or surface lattice oxygen on the sample. In the Mars-van Krevelen mechanism, the first step was dissociative adsorption of the C–Cl bonds at the Lewis acid sites and the dissociatively adsorbed 1,2-DCE was oxidized by the surface O_{latt} species, then a sequential dehydrochlorination and chlorination were the main reaction processes for formation of C₂H₃Cl, and finally the adsorbed oxygen species (with the strong oxidizing ability) on the sample rapidly oxidized the formed intermediates to CO₂ and H₂O.

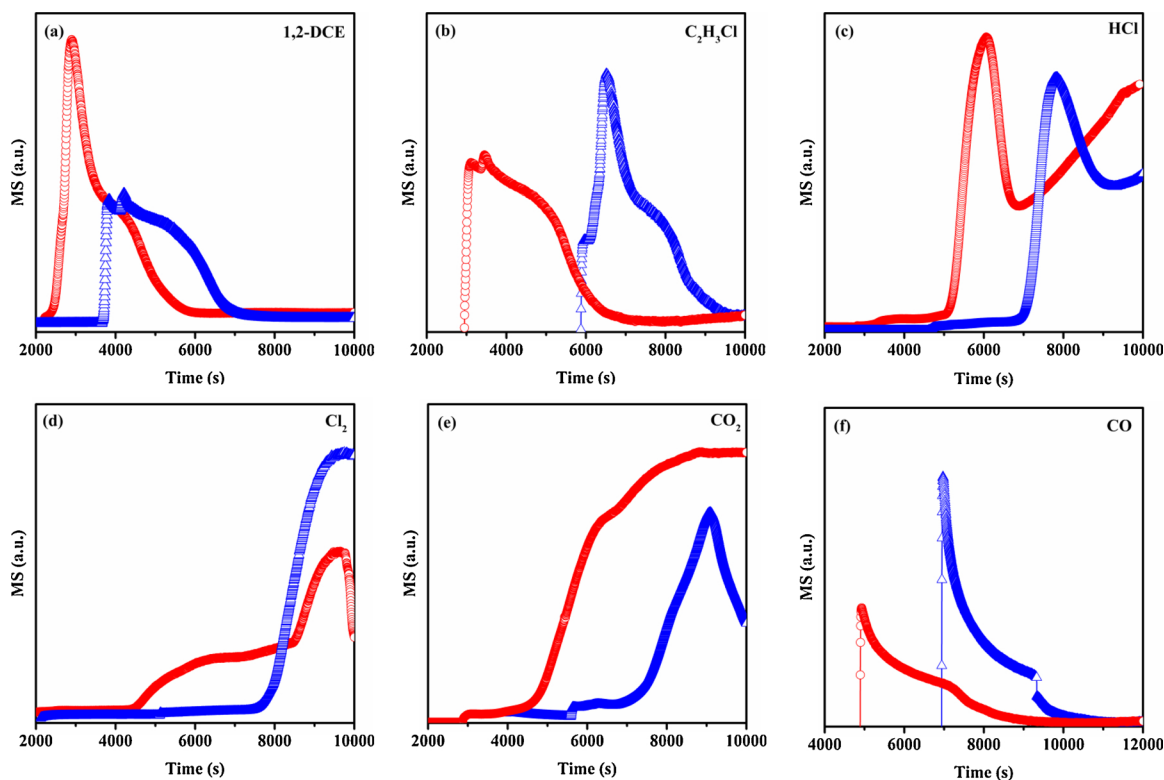


Fig. 13. TPSR profiles of (Δ) TiO₂ and (○) 10CrO_x-TiO₂ during 1,2-DCE oxidation at SV = 40,000 mL/(g h).

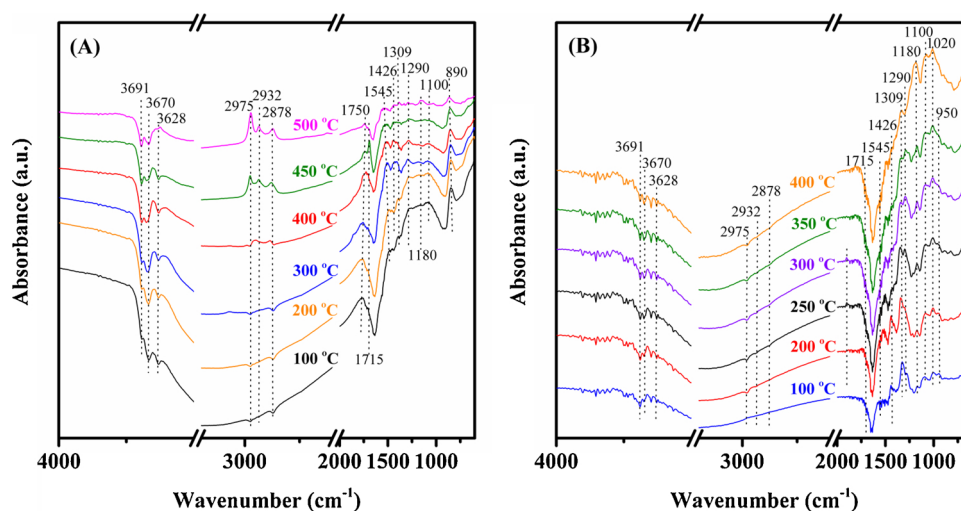


Fig. 14. In situ DRIFTS spectra of (A) TiO_2 and (B) $10\text{CrO}_x\text{-TiO}_2$ during 1,2-DCE oxidation at different temperatures.

4. Conclusions

The $10\text{MO}_x\text{-TiO}_2$ samples were prepared by the coprecipitation method. The MO_x was highly distributed in the $10\text{MO}_x\text{-TiO}_2$ samples. Among all of the $\text{MO}_x\text{-TiO}_2$ samples, $10\text{CrO}_x\text{-TiO}_2$ possessed the best low-temperature reducibility, highest O_{ads} species concentration, and the strongest O_{latt} mobility. The acidic and basic sites were significantly resistant to Cl-adsorption. The $10\text{CrO}_x\text{-TiO}_2$ sample performed the best catalytic activity for 1,2-DCE oxidation ($T_{90\%} = 284\text{ }^\circ\text{C}$; reaction rate = $2.35 \times 10^{-7} \text{ mol}/(\text{g}_{\text{cat}} \text{ s})$ at $260\text{ }^\circ\text{C}$). Meanwhile, the $10\text{CrO}_x\text{-TiO}_2$ sample exhibited good thermal and hydrothermal stability and good HCl-resistant performance. Oxidation of 1,2-DCE obeyed a Mars-van Krevelen mechanism. The good catalytic performance of $10\text{CrO}_x\text{-TiO}_2$ was associated with the synergism of strong acidity, good redox ability, high O_{ads} species concentration, and strong interaction between TiO_2 and MO_x .

Author contribution statement

Mr. Xing Zhang prepared the catalysts, evaluated the activities, and made characterization of XRD, SEM, TEM, HAADF-STEM, BET, $\text{O}_2\text{-TPD}$, and $\text{H}_2\text{-TPR}$; Drs. Yuxi Liu and Jiguang Deng examined the effect of treatment temperature on activity of the typical samples; Dr. Lin Jing, Mr. Zhuo Han, and Miss Xiaohui Yu did the XPS and FT-IR characterization and examined the effects of SV, H_2O , CO_2 , and SO_2 ; and Prof. Hongxing Dai was responsible for the whole work.

Declaration of Competing Interest

The authors declare that they have no known competing financial interests or personal relationships that could have appeared to influence the work reported in this paper.

Acknowledgements

This work was supported by the National Natural Science Foundation of China (21677004, 21876006, 21607005, 21622701, and U1507108), Foundation on the Creative Research Team Construction Promotion Project of Beijing Municipal Institutions (IDHT20190503), and Scientific Research Base Construction—Science and Technology Creation Platform—National Materials Research Base Construction.

Appendix A. Supplementary data

Supplementary material related to this article can be found, in the

online version, at doi:<https://doi.org/10.1016/j.cattod.2019.12.011>.

References

- [1] Q.G. Dai, J.Y. Wu, W. Deng, J.S. Hu, Q.Q. Wu, L.M. Guo, W. Sun, W.C. Zhan, X.Y. Wang, *Appl. Catal. B* 249 (2019) 9–18.
- [2] C. Du, S. Lu, Q. Wang, A.G. Buekens, M. Ni, D.P. Debecker, *Chem. Eng. J.* 334 (2018) 519–544.
- [3] R.J. Xie, J. Ji, K.H. Guo, D.X. Lei, Q.J. Fan, D.Y.C. Leung, H.B. Huang, *Chem. Eng. J.* 356 (2019) 632–640.
- [4] R.M. Fang, H.B. Huang, J. Ji, M. He, Q.Y. Feng, Y.J. Zhan, D.Y.C. Leung, *Chem. Eng. J.* 334 (2018) 2050–2057.
- [5] X. Zhang, Y.X. Liu, J.G. Deng, K.F. Zhang, J. Yang, Z. Han, H.X. Dai, *Catalysts* 8 (2018) 666.
- [6] L.C.A. Oliveira, M.F. Portilho, A.C. Silva, H.A. Taroco, P.P. Souza, *Appl. Catal. B* 117–118 (2012) 29–35.
- [7] Y.F. Gu, X.X. Jiang, W. Sun, S.X. Bai, Q.G. Dai, X.Y. Wang, *ACS Omega* 3 (2018) 8460–8470.
- [8] Q.Y. Chen, N. Li, M.F. Luo, J.Q. Lu, *Appl. Catal. B* 127 (2012) 159–166.
- [9] Y.J. Lao, N.X. Zhu, X.X. Jiang, J. Zhao, Q.G. Dai, X.Y. Wang, *Catal. Sci. Technol.* 8 (2018) 4797–4811.
- [10] Q.G. Dai, S.X. Bai, H. Li, W. Liu, X.Y. Wang, G.Z. Lu, *Appl. Catal. B* 168–169 (2015) 141–155.
- [11] P. Yang, S.S. Yang, Z.N. Shi, Z.H. Meng, R.X. Zhou, *Appl. Catal. B* 162 (2015) 227–235.
- [12] P. Yang, S.F. Zuo, Z.N. Shi, F. Tao, R.X. Zhou, *Appl. Catal. B* 191 (2016) 53–61.
- [13] Y.C. Wei, X.X. Wu, Y.L. Zhao, L. Wang, Z. Zhao, X.T. Huang, J. Liu, J.M. Li, *Appl. Catal. B* 236 (2018) 445–457.
- [14] Z.N. Shi, P. Yang, F. Tao, R.X. Zhou, *Chem. Eng. J.* 295 (2016) 99–108.
- [15] P. Yang, X.M. Xue, Z.H. Meng, R.X. Zhou, *Chem. Eng. J.* 234 (2013) 203–210.
- [16] Z.X. Wu, J.G. Deng, S.H. Xie, H.G. Yang, X.T. Zhao, K.F. Zhang, H.X. Lin, H.X. Dai, G.S. Guo, *Microporous Mesoporous Mater.* 224 (2016) 311–322.
- [17] X.M. Liao, W. Chu, X.Y. Dai, V. Pitchon, *Appl. Catal. A* 449 (2012) 131–138.
- [18] M.H. Kim, K.H. Choo, *Catal. Commun.* 8 (2007) 462–466.
- [19] J. Li, Y.X. Han, Y.H. Zhu, R.X. Zhou, *Appl. Catal. B* 108–109 (2011) 72–80.
- [20] H. Huang, Y.F. Gu, J. Zhao, X.Y. Wang, *J. Catal.* 326 (2015) 54–68.
- [21] K.D. Chen, S.B. Xie, A.T. Bell, E. Iglesia, *J. Catal.* 198 (2001) 232–242.
- [22] C. Li, K. Domen, K. Maruya, T. Onishi, *J. Am. Chem. Soc.* 111 (1989) 7683–7687.
- [23] Q.G. Dai, Z.Y. Zhang, J.R. Yan, J.Y. Wu, G. Johnson, W. Sun, X.Y. Wang, S. Zhang, W.C. Zhan, *Environ. Sci. Technol.* 52 (2018) 13430–13437.
- [24] Y. Wang, A.P. Jia, M.F. Luo, J.Q. Lu, *Appl. Catal. B* 165 (2015) 477–486.
- [25] W. Deng, Q.G. Dai, Y.J. Lao, B.B. Shi, X.Y. Wang, *Appl. Catal. B* 181 (2016) 848–861.
- [26] M.J. Tian, M.D. Ma, B.T. Xu, C.W. Chen, C. He, Z.P. Hao, R. Albilal, *Catal. Sci. Technol.* 8 (2018) 4503–4514.
- [27] S.H. Xie, Y.X. Liu, J.G. Deng, X.T. Zhao, J. Yang, K.F. Zhang, Z. Han, H.X. Dai, *J. Catal.* 342 (2016) 17–26.
- [28] X.W. Xie, Y. Li, Z.Q. Liu, M. Haruta, W.J. Shen, *Nature* 458 (2009) 746–749.
- [29] D.C. Kim, S.K. Ihm, *Environ. Sci. Technol.* 35 (2001) 222–226.
- [30] S.D. Yim, I.S. Num, *J. Catal.* 221 (2004) 601–611.
- [31] X.L. Guo, Z.H. Qiu, J.X. Mao, R.X. Zhou, *Phys. Chem. Chem. Phys.* 20 (2018) 25983–25994.
- [32] M.Q. Yao, N. Wang, W.C. Hua, S. Komarneni, *Appl. Catal. B* 233 (2018) 226–233.
- [33] S.H. Xie, Y.X. Liu, J.G. Deng, X.T. Zhao, J. Yang, K.F. Zhang, Z. Han, H. Arandiyán, H.X. Dai, *Appl. Catal. B* 206 (2017) 221–232.
- [34] T. Yamashita, P. Hayes, *Appl. Surf. Sci.* 254 (2008) 2441–2449.
- [35] R.H. Ma, P.J. Hu, L.Y. Jin, Y.J. Wang, J.Q. Lu, M.F. Luo, *Catal. Today* 175 (2011) 598–602.
- [36] Q.G. Dai, W. Wang, X.Y. Wang, G.Z. Lu, *Appl. Catal. B* 203 (2017) 31–42.
- [37] X. Zhang, Y.X. Liu, J.G. Deng, X.H. Yu, Z. Han, K.F. Zhang, H.X. Dai, *Appl. Catal. B* 257 (2019) 117879.
- [38] P.S. Chintawar, H.L. Greene, *J. Catal.* 165 (1997) 12–21.
- [39] M.J. Tian, C. He, Y.K. Yu, H. Pan, L. Smith, Z.Y. Jiang, N.B. Gao, Y.F. Jian, Z.P. Hao, Q. Zhu, *Appl. Catal. A* 553 (2018) 1–14.